

Article

Structural Origin of the Enhanced Glass-Forming Ability Induced by Microalloying Y in the ZrCuAl Alloy

Gu-Qing Guo, Shi-Yang Wu and Liang Yang *

College of Materials Science and Technology, Nanjing University of Aeronautics and Astronautics, Nanjing 210016, China; guoqing@nuaa.edu.cn (G.-Q.G.); shiyangwu0914@gmail.com (S.-Y.W.)

* Correspondence: yangliang@nuaa.edu.cn; Tel.: +86-25-5211-2903; Fax: +86-25-5211-2626

Academic Editor: Ana Sofia Ramos

Received: 16 January 2016; Accepted: 17 March 2016; Published: 23 March 2016

Abstract: In this work, the structural origin of the enhanced glass-forming ability induced by microalloying Y in a ZrCuAl multicomponent system is studied by performing synchrotron radiation experiments combined with simulations. It is revealed that the addition of Y leads to the optimization of local structures, including: (1) more Zr-centered and Y-centered icosahedral-like clusters occur in the microstructure; (2) the atomic packing efficiency inside clusters and the regularity of clusters are both enhanced. These structural optimizations help to stabilize the amorphous structure in the ZrCuAlY system, and lead to a high glass-forming ability (GFA). The present work provides an understanding of GFAs in multicomponent alloys and will shed light on the development of more metallic glasses with high GFAs.

Keywords: metallic glasses; microalloying; glass-forming ability; synchrotron radiation; microstructure; reverse Monte-Carlo simulation

1. Introduction

In principle, liquid cooled as rapidly as possible can transform into a solid having a glassy structure. For the metallic glass (MG) systems, the minimum cooling rate required for glass forming ranges from 10^{-1} K/s up to 10^6 K/s [1], which sets the good glass forming ability (GFA) systems apart from the marginal systems. Searching for optimized compositions with good GFA, particularly in multicomponent MGs, has been attracting a lot of effort over decades, but so far it is still largely based on a strategy of trial and error in a multidimensional composition space without the effective guidance of any general theory [2–9]. It has been realized that the GFA is extremely sensitive to composition [10,11]. Based on this phenomenon, a practical empirical rule called “microalloying” [12,13] has been widely used to facilitate the development of new MGs with improved GFA [14–17]. Nevertheless, the mechanism of the microalloying effect on GFA remains elusive.

Understanding the GFA of amorphous alloys from the structural perspective has been pursued for decades [18–20]. Although drawing the explicit overall structural picture of MGs has not been solved, local atomic and/or cluster structural models have been proposed by building and stacking clusters to fill space efficiently, including the hard-sphere random-packing model [21], the stereochemically designed model [22], the cluster packing model [23], and the quasi-equivalent clusters model [24]. These structural models can statistically describe the so-called short-to-medium range order in MGs with simple compositions very well. Experiments revealed that the microalloying-enhanced GFA of multicomponent alloys usually has a local maximum in a pinpoint composition [11]. This is associated with fine structural changes in such pinpoint composition [25] which however could not be well described by using the existing theoretical structure models. Therefore, further studies are required to address this issue.

In this work, a feasible scheme for addressing this issue is developed by performing a series of state-of-the-art synchrotron radiation-based experiments combined with simulations to investigate the microstructures of amorphous alloys. We choose the representative CuZrAlY quaternary alloy system as a research prototype. In this system, 5 at. % yttrium addition to CuZrAl mother alloy dramatically increases the critical casting size of the alloy from 3 to 10 mm [14], indicating the microalloying Y-induced increase of GFA.

2. Experimental Section

$\text{Cu}_{46}\text{Zr}_{47}\text{Al}_7$ ternary and corresponding $\text{Cu}_{46}\text{Zr}_{42}\text{Al}_7\text{Y}_5$ quaternary alloy ingots were prepared by arc melting mixtures of Cu (99.9 wt. %), Zr (99.9 wt. %), Al (99.9 wt. %), and Y (99.9 wt. %) in Ti-gettered high-purity argon atmosphere. Amorphous ribbons with a cross section of $0.04 \times 2 \text{ mm}^2$ were produced from these ingots via single-roller melt spinning at a wheel surface velocity of 40 m/s in purified Ar atmosphere. Firstly, X-ray diffraction (Cu K_{α} , radiation) was performed to confirm the amorphous state of the as-prepared samples. Subsequently, room temperature X-ray diffraction (XRD) measurement was performed using a high-energy synchrotron radiation monochromatic beam (about 100 keV) on beam line BW5 in HasyLab, Germany. Two-dimensional diffraction data was collected by a Mar345 image plate and then was integrated to Q -space by subtracting the background using the program Fit2D [26]. The output data was normalized by PDFgetX software to obtain structure factor $S(Q)$ according to the Faber-Ziman equation [27]. Furthermore, extended X-ray absorption fine structure (EXAFS) measurements for Zr, Cu, and Y K-edge were carried out using transmission mode at beam lines BL14W1 in the Shanghai Synchrotron Radiation Facility of China and U7C in the National Synchrotron Radiation Laboratory of China. Because of the experimentally-inaccessible energy value of the Al K-edge (1.560 keV), EXAFS did not allow the measurement of the local structure around the Al atoms. These EXAFS raw data were normalized via a standard data-reduced procedure, employing the Visual Processing in EXAFS Researches [28].

In order to obtain the atomic structural information as reliably as possible, both the normalized diffraction and EXAFS data were simulated simultaneously under the framework of reverse Monte-Carlo (RMC) [29]. Cubic boxes we used in the RMC simulation contained 40,000 atoms, matching $\text{Cu}_{46}\text{Zr}_{42}\text{Al}_7\text{Y}_5$ and $\text{Cu}_{46}\text{Zr}_{47}\text{Al}_7$ compositions. During RMC simulation, atoms move randomly within a determined time interval. The experimental data are compared to the simulation with an iterative calculation [30]:

$$\delta^2 = \frac{1}{\varepsilon^2} \sum_n (S_m(Q_n) - S_{\text{exp}}(Q_n))^2 + \frac{1}{\varepsilon_i^2} \sum_n (\chi_{m,El}(\kappa_n) - \chi_{\text{exp},El}(\kappa_n))^2 \quad (1)$$

where δ^2 represents the deviation between the experimental and simulation data, ε parameters regulate the weight of the data set given in the fitting procedure, E_i denotes Ni, Nb, and Zr elements, and $S(Q)$ and $\chi(k)$ parameters are the XRD structural factor in Q space and the EXAFS signal, respectively. The subscripts "m" and "exp" represent the simulations and the experiments, respectively. The theoretical EXAFS signal, $\chi(k)$, of the i th element is calculated from the following equation:

$$\chi_{m,i}(\kappa) = \sum_j 4\pi c_j \rho \int r^2 \gamma_{ij}(r, \kappa) g_{ij}(r) dr \quad (2)$$

where c_j is the concentration of the j th element and γ_{ij} can be calculated by:

$$\gamma_{ij}(r, \kappa) = A_{ij}(\kappa, r) \sin(2\kappa r + \Phi_{ij}(\kappa r)) \quad (3)$$

where A_{ij} and Φ_{ij} denote the amplitude and the phase shift, respectively. They can be obtained by using the FEFF 8.1 code [30].

It should be noted that although during RMC simulation, the simulated experimental data do not include the Al K-edge EXAFS, we can still get reliable structural information, for the following reasons: (1) EXAFS is an element-specific method available for measuring the surroundings of each kind of atom. In other words, all the neighbor atoms around each atom can be distinguished when EXAFS data is fitted or simulated [31]. Since Zr, Cu, and Y EXAFS data can reflect all of their neighborhood information containing Zr, Cu, Y, and Al atoms, how the Al atoms distribute around the Zr (Cu or Y) centers can be determined accordingly; (2) four independent sets of experimental data (one set of XRD and three sets of EXAFS (Zr, Cu, and Y)) were simultaneously simulated in this work. During the RMC simulation, all of these experimental data should fit their counterparts calculated theoretically from the same structural model. Such constraint can eliminate the computational randomness. Additionally, the RMC-simulated atomic structural models were further analyzed by the Voronoi tessellation method [32].

3. Results and Discussion

Compared with routine lab experiments (such as X-ray powder diffraction measurement), the synchrotron radiation-based XRD measurements can provide high-resolution data, which are more reliable for detecting the fine structures in materials, in particular in amorphous alloys. The original two-dimensional diffraction patterns of both $\text{Cu}_{46}\text{Zr}_{42}\text{Al}_7\text{Y}_5$ and $\text{Cu}_{46}\text{Zr}_{47}\text{Al}_7$ samples are plotted in Figure 1a,b. To obtain more accessible structural information, these two-dimensional patterns are transformed into one-dimensional curves. Figure 1c,d shows the corresponding one-dimensional structural factor. The amorphous nature of both samples can be confirmed because there are no circle lines or dots in the two-dimensional diffraction patterns and no sharp Bragg peaks behind the first strong peak in the structural factor curves, while these features are usually observed in the diffraction data of polycrystals or single crystals [33].

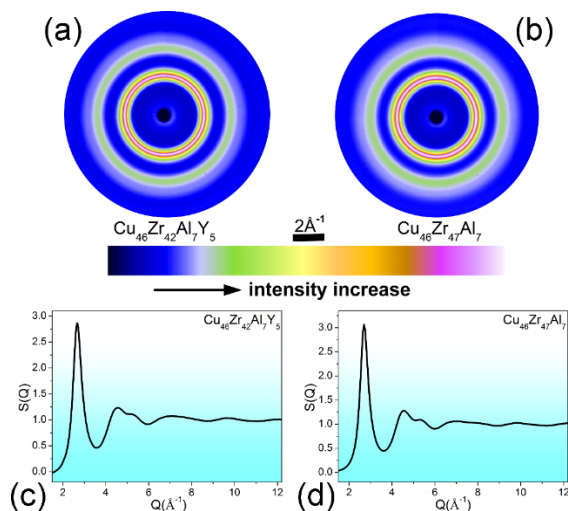


Figure 1. The two-dimensional X-ray diffraction (XRD) patterns in (a) $\text{Cu}_{46}\text{Zr}_{42}\text{Al}_7\text{Y}_5$ and (b) $\text{Cu}_{46}\text{Zr}_{47}\text{Al}_7$ amorphous samples; and the deduced data, including: the structural factors ($S(Q)$ s) of (c) $\text{Cu}_{46}\text{Zr}_{42}\text{Al}_7\text{Y}_5$ and (d) $\text{Cu}_{46}\text{Zr}_{47}\text{Al}_7$. To highlight oscillations in low Q region of $S(Q)$, the Q region here was shortened to about 12 \AA^{-1} .

Figure 2a–d shows the XRD and EXAFS experimental data as well as their corresponding RMC simulated curves. To ensure the proper interpretation of all the structural information during normalization, the EXAFS data for Zr, Cu, and Y K-edge were weighted by κ^3 values. This does not reduce the reliability of RMC simulation, because all the simulated Zr, Cu, and Y K-edge EXAFS spectra also are strictly weighted by κ^3 values, so that no systematic errors will be generated [28].

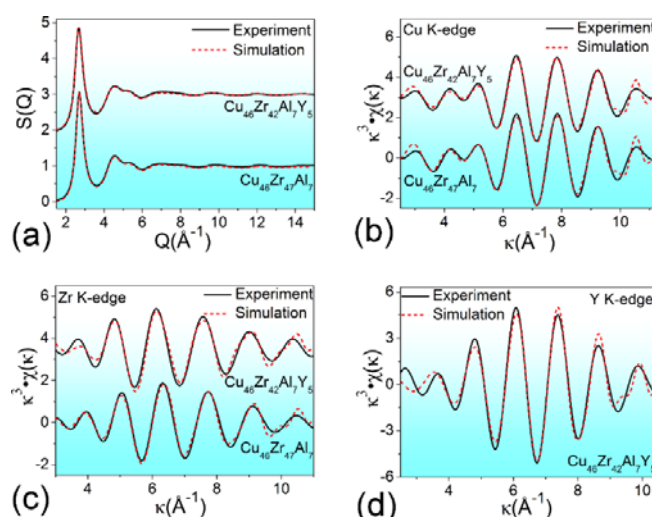


Figure 2. XRD and extended X-ray absorption fine structure (EXAFS) experimental data as well as their corresponding simulated curves, including (a) $S(Q)$; (b) Cu K-edge, (c) Zr K-edge, and (d) Y K-edge EXAFS data. Experimental and simulated data are plotted with the solid and the dashed lines, respectively. All the experimental and the simulated signals were weighted by κ^3 . To highlight the $S(Q)$ difference between the experimental and the simulated data for both samples, the Q region here was shortened to about 15 \AA^{-1} .

The good matching between all the experiment/simulation pairs confirms the success of the RMC simulations. Based on the simulated structural models, atomic-level structural information can be deduced. The coordination numbers (CNs) around Zr, Cu, Al, and Y center atoms, as well as all kinds of atomic-pair distances, are listed in Table 1.

Table 1. The first-shell atomic-pair information deduced from the reverse Monte-Carlo (RMC)-simulated structural models of $\text{Cu}_{46}\text{Zr}_{42}\text{Al}_7\text{Y}_5$ and $\text{Cu}_{46}\text{Zr}_{47}\text{Al}_7$ samples, including coordination numbers (CNs) and atomic-pair distances (R). Note that M denotes Cu, Zr, Al, or Y. The Goldschmidt radii of Zr, Cu, Y, and Al are 1.60 \AA , 1.28 \AA , 1.80 \AA , and 1.43 \AA , respectively.

Atomic Pairs	$\text{Cu}_{46}\text{Zr}_{47}\text{Al}_7$			$\text{Cu}_{46}\text{Zr}_{42}\text{Al}_7\text{Y}_5$		
	$R(\text{\AA}) \pm 0.01$	CNs	Uncertainty of CNs	$R(\text{\AA}) \pm 0.01$	CN	Uncertainty of CNs
Cu-Cu	2.59	5.0	± 0.2	2.60	5.3	± 0.3
Cu-Zr	2.88	5.4	± 0.3	2.89	4.2	± 0.3
Cu-Al	2.61	0.7	+0.3, -0.1	2.60	0.7	+0.2, -0.1
Cu-Y	-	-	-	2.98	0.9	-
Cu-M	-	11.1	-	-	11.1	-
Zr-Cu	2.88	5.4	± 0.2	2.89	5.5	± 0.2
Zr-Zr	3.20	5.9	± 0.2	3.20	5.3	± 0.3
Zr-Al	2.82	0.8	+0.2, -0.1	2.79	0.7	+0.3, -0.1
Zr-Y	-	-	-	3.54	0.5	+0.1
Zr-M	-	12.1	-	-	12.0	-
Al-Cu	2.61	4.9	± 0.2	2.60	5.5	± 0.3
Al-Zr	2.82	5.7	± 0.3	2.79	4.9	± 0.2
Al-Al	2.70	0.1	+0.1	2.70	0.1	+0.1
Al-Y	-	-	-	3.29	0.2	+0.2
Al-M	-	10.7	-	-	10.7	-
Y-Cu	-	-	-	2.98	7.7	± 0.4
Y-Zr	-	-	-	3.54	4.5	± 0.3
Y-Al	-	-	-	3.29	0.2	+0.2
Y-Y	-	-	-	3.76	0.3	+0.1
Y-M	-	-	-	-	12.7	-

For CN values, it is shown that there are obvious CN decreases in Cu-Zr and Al-Zr atomic pairs from $Zr_{47}Cu_{46}Al_7$ to $Zr_{42}Cu_{46}Y_5Al_7$ (5.4 to 4.2 and 5.7 to 4.9). In previous work, separation between Y and Zr was suggested due to the positive heat of mixing between Y and Zr [34]. Therefore, Y and Zr atoms are prone to avoid each other, and Cu and Al atoms are expected to favor more Y atoms and less Zr atoms. In addition, it seems that Y addition does not induce a change of the total CNs of Zr, Cu, and Al centers. In both samples, the CN of Zr centers is about 12, while the CNs around Cu and Al centers are only 11 and 10.7, respectively. The CN around Al centers is a relatively small value. In previous work [35], it has been revealed that there is a bond shortening for Al-connected atomic pairs. This leads to fewer neighbor atoms around the Al centers. For atomic-pair distances, Zr-Zr, Zr-Cu, Cu-Cu, and some other atomic pairs have almost the same values in both samples. Nevertheless, it is found that the Zr-Y distance (3.54 Å) is obviously larger than the sum of Zr and Y Goldschmidt radii ($1.60 + 1.80 = 3.40$ Å), indicating the relatively weak interaction between the Zr-Y pair. From the atomic-level structural information mentioned above, we can conclude that Y doping does tune the local structures, but how Y doping affects the GFA needs to be further studied.

We can obtain cluster-level structural information via the Voronoi-tessellation approach. In other words, Voronoi clusters (VCs) can be extracted from the RMC simulated structural models, and indexed based on their geometrical features. The major VCs centered with Zr, Cu, Y, and Al atoms are plotted in Figure 3a–d. The ideal icosahedral cluster ($\langle 0,0,12,0 \rangle$) and the icosahedral-like VCs ($\langle 0,2,8,2 \rangle$, $\langle 0,3,6,3 \rangle$, and $\langle 0,4,4,4 \rangle$) whose CN are 12 have been proved to be the favorite structural units in the microstructures of MGs [36–38]. As shown in Figure 3, the major Cu-, Zr-, Al-, and Y-centered VCs (whose fractions are larger than 2% are selected) have broad CN distributions ranging from 9 to 13, 11 to 15, 8 to 12, and 10 to 14, respectively. Take Figure 3b for example, the popular Zr-centered VCs are 12-CN ones ($\langle 0,2,8,2 \rangle$ and $\langle 0,3,6,3 \rangle$) and 13-CN ones ($\langle 0,1,10,2 \rangle$ and $\langle 0,3,6,4 \rangle$), while none of them has a fraction higher than 16%. This indicates that various clusters co-existing to form the microstructure is the intrinsic structural feature in glassy alloys [39], and icosahedral clusters are the preferred but not the only clusters favored in the glassy structure, because only stacking icosahedral clusters can not fill space completely [39]. In addition, the Zr-centered icosahedral-like VCs in both samples have high weights, while fractions of the Cu-centered icosahedral-like counterparts are relatively small, let alone the Al-centered ones. This implies that the Zr-centered icosahedral-like VCs rather than Cu- or Al-centered counterparts contribute to the glass formation in $Cu_{46}Zr_{42}Al_7Y_5$ and $Cu_{46}Zr_{47}Al_7$ compositions. In addition, compared with $Cu_{46}Zr_{47}Al_7$, there are higher fractions of these icosahedral-like VCs (such as $\langle 0,2,8,2 \rangle$ and $\langle 0,3,6,3 \rangle$) and lower weights of non-icosahedral VCs (such as $\langle 0,1,10,2 \rangle$ and $\langle 0,3,6,4 \rangle$) in $Cu_{46}Zr_{42}Al_7Y_5$. Especially, the Zr-centered icosahedral clusters in $Cu_{46}Zr_{42}Al_7Y_5$ have a total fraction about 30%. This illustrates that when 5 at. % Y is added, Zr-centered icosahedral-like local structures became more popular in the microstructure. Furthermore, it is worth noting that the Y-centered icosahedral-like VCs possess relatively high proportions, which are even higher than the Zr-centered counterparts. Since Y atoms are the substitutes of Zr ones, it implies that the ZrCuAlY quaternary MG contains more icosahedral-like VCs than the corresponding ZrCuAl ternary sample, contributing to the higher GFA in the former.

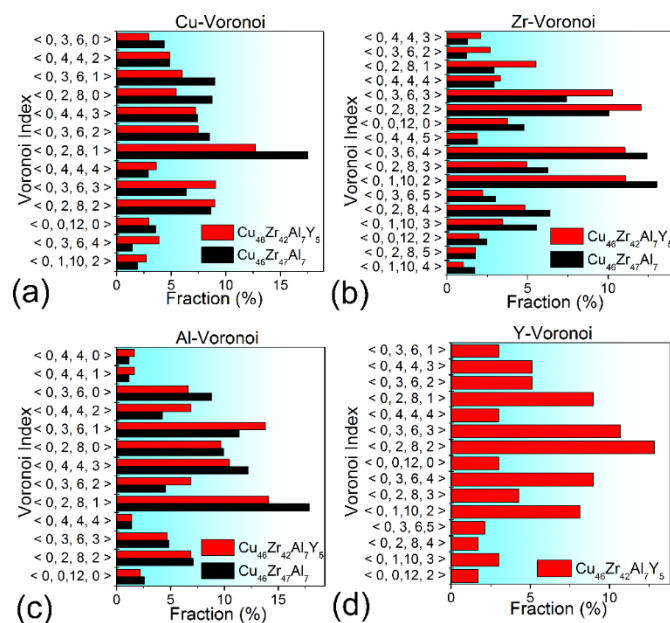


Figure 3. Distribution of the major Voronoi clusters (VCs), including: (a) Cu-centered VCs; (b) Zr-centered VCs; (c) Al-centered VCs; and (d) Y-centered VCs. Only those whose fractions are larger than 2% are selected. The CN value denotes the number of shell atoms of the corresponding VC; *i.e.*, the CN around the center atom.

Changing the configuration of one cluster while keeping its indexed character can apparently change the packing of atoms inside this cluster. In our previous work, it has been pointed out that the atomic packing efficiency inside clusters strongly relates to the GFA in binary alloys [25]. This is consistent with the widely-accepted dense packing principle [40,41]. The atomic packing efficiency can be calculated by

$$\text{APE} = V_a/V_u \quad (4)$$

where V_a and V_u denote the volume of atoms contained in clusters and the total volume of clusters themselves, respectively. V_u can be obtained by summing the volumes of all the tetrahedra in VCs because each VC is built by stacking tetrahedra with a shared vertex, located at the site of the VC's center atom. Because each atom embedded in the cluster is truncated as a cone ball, V_a can be calculated by summing the volumes of all the cone balls [25]. Because bond shortening around Al atoms in ZrCuAl MG was found in previous work [35], the atomic radius of the Al atom (1.26 Å) is estimated by

$$r_{\text{Al}} = \frac{CN_{\text{Al-Cu}} \times (d_{\text{Cu-Al}} - r_{\text{Cu}}) + CN_{\text{Al-Zr}} \times (d_{\text{Zr-Al}} - r_{\text{Zr}})}{CN_{\text{Al-Cu}} + CN_{\text{Al-Zr}}} \quad (5)$$

where r_{Al} is the Al atomic radius, $CN_{\text{Al-Cu}}$ and $CN_{\text{Al-Zr}}$ stand for the numbers of Zr and Cu atoms around Al centers, respectively. In addition, $d_{\text{Cu-Al}}$ and $d_{\text{Al-Zr}}$ denote the distances of Al-Cu and Al-Zr pairs, respectively. For Zr, Cu, and Y atoms, because their neighbors are almost Cu and Zr atoms, and there are not strong bondings in Zr-Zr, Zr-Cu, Zr-Y, Cu-Y pairs, so that Zr, Cu, and Y atomic radii are the half of Zr-Zr, Cu-Cu, and Y-Y bond lengths, respectively (*i.e.*, 1.60 Å, 1.30 Å, and 1.78 Å). The average atomic packing efficiency values of both samples are plotted in Figure 4. It is obvious that the atomic packing efficiency of $\text{Cu}_{46}\text{Zr}_{42}\text{Al}_7\text{Y}_5$ has a higher value than that of $\text{Cu}_{46}\text{Zr}_{47}\text{Al}_7$. This indicates that Y addition not only changes the geometrical index of clusters, but also tunes the atomic packing inside these clusters, leading to a denser packing.

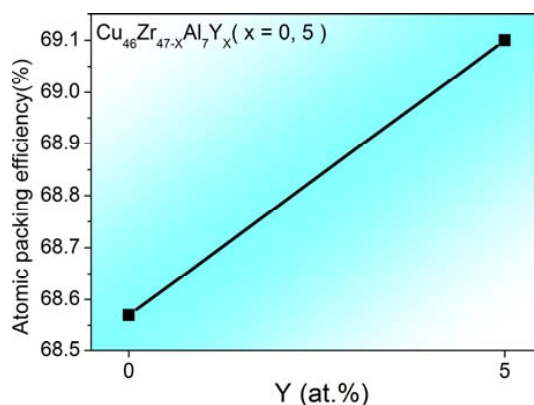


Figure 4. Atomic packing efficiency values of $\text{Cu}_{46}\text{Zr}_{42}\text{Al}_7\text{Y}_5$ and $\text{Cu}_{46}\text{Zr}_{47}\text{Al}_7$ samples.

Furthermore, the VC's shape strongly depends on the "stoichiometry" of its containing atoms, due to the atomic radial diversity among heterogeneous atoms [42]. As a result, there are different structural regularities in a number of VCs having the same index, let alone VCs with different indexes. For example, the regularity of a $\text{Cu}_6\text{Zr}_5\text{Y}_1\text{Al}_1$ $\langle 0,2,8,2 \rangle$ VC is obviously different from that of another $\text{Cu}_6\text{Zr}_5\text{Y}_1\text{Al}_1$ $\langle 0,2,8,2 \rangle$ counterpart, as shown in Figure 5. In previous work, it was suggested that the regularity of clusters may influence the glass formation in alloys [25,43,44]. Thus, we should know whether or not the regularity of VCs contributes to the GFA of $\text{Cu}_{46}\text{Zr}_{42}\text{Al}_7\text{Y}_5$ and $\text{Cu}_{46}\text{Zr}_{47}\text{Al}_7$.

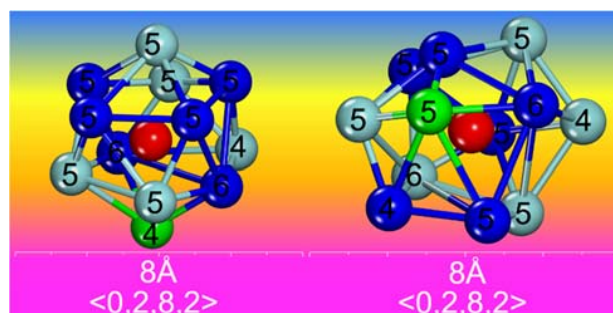


Figure 5. Configurations of two VCs extracted from the RMC-simulated model of $\text{Cu}_{46}\text{Zr}_{42}\text{Al}_7\text{Y}_5$, with the same $\langle 0,2,8,2 \rangle$ index. The number labeled on each shell atom stands for the number of its neighbor (connected) shell atoms, also indicates the i -fold symmetry. The blue, celadon, red, and green balls stand for Cu, Zr, Y, and Al atoms, respectively.

Here, a structural parameter (T) is adopted for indicating the regularity of clusters. T is the differences of all the edge lengths in a tetrahedron. Each VC can be formed by piling up a set of Delaunay tetrahedra which share a common vertex at the center atom of this VC [32], so that the regularity of their containing tetrahedra can be examined and extrapolated to any given VCs. T can be calculated by

$$T = \sum_{i \neq j} (e_i - e_j)^2 / 15 < e >^2 \quad (6)$$

where e_i denotes the length of the i th edge on the triangle face of a given tetrahedron, and $\langle e \rangle$ is the corresponding mean value. For a regular tetrahedron where all edges are the same, the value of T should be zero. Thus, if a tetrahedron has a smaller T value, it has a higher regularity. The average T values in both samples are plotted in Figure 6. It is worth noting that $\text{Cu}_{46}\text{Zr}_{42}\text{Al}_7\text{Y}_5$ has a lower T value than $\text{Cu}_{46}\text{Zr}_{47}\text{Al}_7$. This indicates that when microalloying Y in the ZrCuAl alloy, the configurations of clusters are modified due to the denser atomic packing, exhibiting a higher degree of regularity.

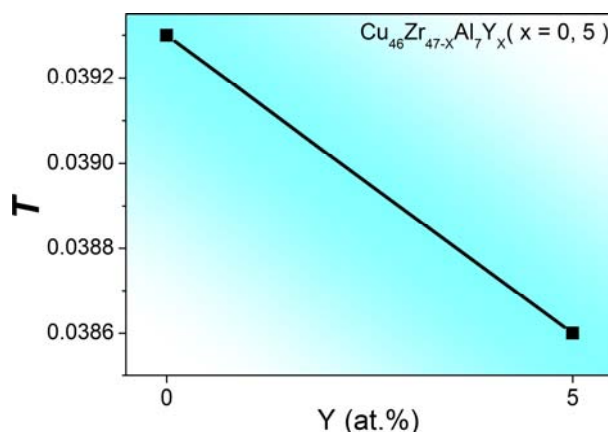


Figure 6. Variance of the edge lengths (T) of all the tetrahedra forming VCs in $\text{Cu}_{46}\text{Zr}_{42}\text{Al}_7\text{Y}_5$ and $\text{Cu}_{46}\text{Zr}_{47}\text{Al}_7$. This value determines the regularity of VCs.

In previous work, the GFA dependence on Y addition has been studied from thermodynamic or kinetic aspects [14,45]. In this work, we try to address this issue from the microstructure aspect. According to the numerous atomic- and cluster-level structural features and factors deduced above, we can analyze the reason why minor Y addition significantly affects the GFA in the ZrCuAl alloy system. It has been revealed in previous work [35] that in CuZrAl ternary composition, local structures centered with Zr and Cu solvents (major VCs) establish the structural basis, and Al solutes mainly play the role of connecting these major VCs to fill the space. In particular, the Zr atoms are apt to enter the center site of icosahedra, whereas the Cu-centered icosahedral-like VCs have a relatively low fraction.

When minor Y atoms (5 at. % in our case) are doped to replace Zr atoms, although the average CN around Zr atoms does not change, the fraction of icosahedral-like VCs with Zr centers increases. In addition, Y atoms are more likely to enter the center sites of icosahedral-like VCs. Therefore, more icosahedral-like local structures exist in the $\text{Cu}_{46}\text{Zr}_{42}\text{Al}_7\text{Y}_5$ quaternary MG. In previous work, it has been revealed that icosahedral local structures contribute to the formation of MGs [46,47], because stacking clusters with abundant five-fold point symmetrical features such as icosahedra can result in the exclusion of structural periodicity, which is required in crystals [39]. In this sense, increase of the icosahedral-like clusters leads to stabilization of the amorphous microstructure in the $\text{Cu}_{46}\text{Zr}_{42}\text{Al}_7\text{Y}_5$ alloy, greatly enhancing the GFA. Moreover, Y addition tunes the connections between heterogeneous atoms, leading to higher atomic packing inside clusters and a higher degree of regularity of clusters. Such optimization of local structures also contributes to the stabilization of the amorphous microstructure.

In one recent article studying the microalloying effect on the glass formation and the mechanical properties of MGs [48], the authors present a theory built around the experimental evidence that the microalloying elements organize a neighborhood around them that differs from both the crystalline and the glassy phases of the material in the absence of the additional elements. They also claim that a minute amount of foreign atoms (the so-called pinpoint effect [11]) influencing the GFA can be predicted by their theory. In our work studying the microalloying effect on the GFA in a ZrCuAl system from the microstructure aspect, the microstructural parameters proposed to contribute to glass formation (such as fraction of icosahedral clusters, the atomic packing efficiency, and the regularity of clusters) surely do not increase their values monotonously when adding more Y atoms in a ZrCuAl system. This also can explain why there is a minute amount of (Y) foreign atoms leading to enhancement of the GFA. This indicates that both the theoretical work [48] and our experimental work can shed light on the microalloying effect on the GFAs in multicomponent alloy systems.

4. Conclusions

The microstructures of $\text{Cu}_{46}\text{Zr}_{42}\text{Al}_7\text{Y}_5$ and $\text{Cu}_{46}\text{Zr}_{47}\text{Al}_7$ MGs are investigated by calculations based on the data obtained from synchrotron radiation-based XRD and EXAFS experiments. It is revealed that microalloying Y in the ZrCuAl alloy not only increases the fraction of Zr-centered icosahedral-like local structures, but also enhances the atomic packing efficiency and the regularity of clusters. This stabilizes the glassy-state structure, contributing significantly to the great enhancement of GFA. This study provides an in-depth understanding on how fine structures tune the glass formation in a mass of multicomponent MGs.

Acknowledgments: The authors would like to thank the HASYLAB in Germany, the Shanghai Synchrotron Radiation Facility in China, and the National Synchrotron Radiation Laboratory of China for the use of the advanced synchrotron radiation facilities. Financial supports from the National Natural Science Foundation of China (Grant No. U1332112 and 51471088), the Fundamental Research Funds for the Central Universities (Grant No. NE2015004), the Funding for Outstanding Doctoral Dissertation in NUAA (Grant No. BCXJ12-08), the Funding of Jiangsu Innovation Program for Graduate Education (Grant No. CXLX13-152), and the project funded by the Priority Academic Program Development (PAPD) of Jiangsu Higher Education Institutions are gratefully acknowledged.

Author Contributions: G.-Q.G. performed simulation work upon the experimental data. L.Y. performed analysis of this work and wrote this article. S.-Y.W. contributed to the experimental research work.

Conflicts of Interest: The authors declare no conflict of interest.

References

1. Inoue, A. Stabilization of metallic supercooled liquid and bulk amorphous alloys. *Acta Mater.* **2000**, *48*, 279–306. [[CrossRef](#)]
2. Turnbull, D. Under what conditions can a glass be formed? *Contemp. Phys.* **1969**, *10*, 473–488. [[CrossRef](#)]
3. Greer, A.L. Confusion by Design. *Nature* **1993**, *366*, 303–304. [[CrossRef](#)]
4. Johnson, W.L. Bulk glass-forming metallic alloys: Science and technology. *MRS Bull.* **1999**, *24*, 42–56. [[CrossRef](#)]
5. Lu, Z.P.; Tan, H.; Li, Y.; Ng, S.C. The correlation between reduced glass transition temperature and glass forming ability of bulk metallic glasses. *Scr. Mater.* **2000**, *42*, 667–673. [[CrossRef](#)]
6. Lu, Z.P.; Liu, C.T. Glass formation criterion for various glass-forming systems. *Phys. Rev. Lett.* **2003**. [[CrossRef](#)] [[PubMed](#)]
7. Wang, W.H.; Dong, C.; Shek, C.H. Bulk metallic glasses. *Mater. Sci. Eng. R* **2004**, *44*, 45–89. [[CrossRef](#)]
8. Schroers, J.; Johnson, W.L. Ductile bulk metallic glass. *Phys. Rev. Lett.* **2004**. [[CrossRef](#)] [[PubMed](#)]
9. Ashby, M.F.; Greer, A.L. Metallic glasses as structural materials. *Scr. Mater.* **2006**, *54*, 321–326. [[CrossRef](#)]
10. Na, J.H.; Demetriou, M.D.; Floyd, M.; Hoff, A.; Garrett, G.R.; Johnson, W.L. Compositional landscape for glass formation in metal alloys. *Proc. Natl. Acad. Sci. USA* **2014**, *111*, 9031–9036. [[CrossRef](#)] [[PubMed](#)]
11. Ma, D.; Tan, H.; Wang, D.; Li, Y.; Ma, E. Strategy for pinpointing the best glass-forming alloys. *Appl. Phys. Lett.* **2005**. [[CrossRef](#)]
12. Lu, Z.P.; Liu, C.T. Role of minor alloying additions in formation of bulk metallic glasses: A review. *J. Mater. Sci.* **2004**, *39*, 3965–3974. [[CrossRef](#)]
13. Wang, W.H. Roles of minor additions in formation and properties of bulk metallic glasses. *Prog. Mater. Sci.* **2007**, *52*, 540–596. [[CrossRef](#)]
14. Xu, D.H.; Duan, G.; Johnson, W.L. Unusual glass-forming ability of bulk amorphous alloys based on ordinary metal copper. *Phys. Rev. Lett.* **2004**. [[CrossRef](#)] [[PubMed](#)]
15. Wang, D.; Tan, H.; Li, Y. Multiple maxima of GFA in three adjacent eutectics in Zr-Cu-Al alloy system-A metallographic way to pinpoint the best glass forming alloys. *Acta Mater.* **2005**, *53*, 2969–2979. [[CrossRef](#)]
16. Zhang, Q.S.; Zhang, W.; Inoue, A. Preparation of $\text{Cu}_{36}\text{Zr}_{48}\text{Ag}_8\text{Al}_8$ bulk metallic glass with a diameter of 25 mm by copper mold casting. *Mater. Trans.* **2007**, *48*, 629–631. [[CrossRef](#)]
17. Chen, L.Y.; Fu, Z.D.; Zhang, G.Q.; Hao, X.P.; Jiang, Q.K.; Wang, X.D.; Cao, Q.P.; Franz, H.; Liu, Y.G.; Xie, H.S.; *et al.* New class of plastic bulk metallic glass. *Phys. Rev. Lett.* **2008**. [[CrossRef](#)] [[PubMed](#)]
18. Egami, T.; Waseda, Y. Atomic size effect on the formability of metallic glasses. *J. Non-Cryst. Solids* **1984**, *64*, 113–134. [[CrossRef](#)]

19. Hirata, A.; Guan, P.F.; Fujita, T.; Hirotsu, Y.; Inoue, A.; Yavari, A.R.; Sakurai, T.; Chen, M.W. Direct observation of local atomic order in a metallic glass. *Nat. Mater.* **2011**, *10*, 28–33. [[CrossRef](#)] [[PubMed](#)]
20. Wu, Z.W.; Li, M.Z.; Wang, W.H.; Liu, K.X. Hidden topological order and its correlation with glass-forming ability in metallic glasses. *Nat. Commun.* **2015**. [[CrossRef](#)] [[PubMed](#)]
21. Bernal, J.D. A geometrical approach to the structure of liquids. *Nature* **1959**, *183*, 141–147.
22. Gaskell, P.H. A new structural model for transition metal-metalloid glasses. *Nature* **1978**, *276*, 484–485. [[CrossRef](#)]
23. Miracle, D.B. A structural model for metallic glasses. *Nat. Mater.* **2004**, *3*, 697–702. [[CrossRef](#)] [[PubMed](#)]
24. Sheng, H.W.; Luo, W.K.; Alamgir, F.M.; Bai, J.M.; Ma, E. Atomic packing and short-to-medium-range order in metallic glasses. *Nature* **2006**, *439*, 419–425. [[CrossRef](#)] [[PubMed](#)]
25. Yang, L.; Guo, G.Q.; Chen, L.Y.; Huang, C.L.; Ge, T.; Chen, D.; Liaw, P.K.; Saksl, K.; Ren, Y.; Zeng, Q.S.; *et al.* Atomic-Scale Mechanisms of the Glass-Forming Ability in Metallic Glasses. *Phys. Rev. Lett.* **2012**. [[CrossRef](#)] [[PubMed](#)]
26. Hammersley, A.P.; Svensson, S.O.; Hanfland, M.; Fitch, A.N.; Häusermann, D. Two-dimensional detector software: From real detector to idealised image or two-theta scan. *High Press. Res.* **1996**, *14*, 235–248. [[CrossRef](#)]
27. Qiu, X.; Thompson, J.W. PDFgetX2: A GUI-driven program to obtain the pair distribution function from X-ray powder diffraction data. *J. Appl. Crystallogr.* **2004**, *37*, 110–116. [[CrossRef](#)]
28. Klementev, K.V. Extraction of the fine structure from X-ray absorption spectra. *J. Phys. D* **2001**, *34*, 209–217. [[CrossRef](#)]
29. McGreevy, R.L. Reverse Monte Carlo modelling. *J. Phys. Condens. Matter.* **2001**, *13*, R877–R913. [[CrossRef](#)]
30. Saksl, K.; Jovari, P.; Franz, H.; Zeng, Q.S.; Liu, J.F.; Jiang, J.Z. Atomic structure of Al₈₉La₆Ni₅ metallic glass. *J. Phys. Condens. Matter.* **2006**, *18*, 7579–7592. [[CrossRef](#)] [[PubMed](#)]
31. Ravel, B.; Newville, M. Athena, Artemis, Hephaestus: Data analysis for X-ray absorption spectroscopy using IFEFFIT. *J. Synch. Rad.* **2005**, *12*, 537–541. [[CrossRef](#)] [[PubMed](#)]
32. Medvedev, N.N. The algorithm for three-dimensional Voronoi polyhedral. *J. Comput. Phys.* **1986**, *67*, 223–229. [[CrossRef](#)]
33. Zeng, Q.S.; Sheng, H.W.; Ding, Y.; Wang, L.; Yang, W.G.; Jiang, J.Z.; Mao, W.L.; Mao, H.K. Long-range topological order in metallic glass. *Science* **2011**, *332*, 1404–1406. [[CrossRef](#)] [[PubMed](#)]
34. Park, E.S.; Kim, D.H. Phase separation and enhancement of plasticity in Cu-Zr-Al-Y bulk metallic glasses. *Acta Mater.* **2006**, *54*, 2597–2604. [[CrossRef](#)]
35. Yang, L.; Guo, G.Q.; Chen, L.Y.; Wei, S.H.; Jiang, J.Z.; Wang, X.D. Atomic structure in Al-doped multicomponent bulk metallic glass. *Scr. Mater.* **2010**, *63*, 879–882. [[CrossRef](#)]
36. Wang, S.Y.; Kramer, M.J.; Xu, M.; Wu, S.; Hao, S.G.; Sordelet, D.J.; Ho, K.M.; Wang, C.Z. Experimental and *ab initio* molecular dynamics simulation studies of liquid Al₆₀Cu₄₀ alloy. *Phys. Rev. B* **2009**. [[CrossRef](#)]
37. Yang, L.; Guo, G.Q. Preferred clusters in metallic glasses. *Chin. Phys. B* **2010**. [[CrossRef](#)]
38. Fang, H.Z.; Hui, X.; Chen, G.L.; Liu, Z.K. Al-centered icosahedral ordering in Cu₄₆Zr₄₆Al₈ bulk metallic glass. *Appl. Phys. Lett.* **2009**. [[CrossRef](#)]
39. Guo, G.Q.; Wu, S.Y.; Luo, S.; Yang, L. Detecting Structural Features in Metallic Glass via Synchrotron Radiation Experiments Combined with Simulations. *Metals* **2015**, *5*, 2093–2108. [[CrossRef](#)]
40. Li, Y.; Guo, Q.; Kalb, J.A.; Thompson, C.V. Matching glass-forming ability with the density of the amorphous phase. *Science* **2008**, *322*, 1816–1819.
41. Greer, A.L.; Ma, E. Bulk metallic glasses: At the cutting edge of metals research. *Mater. Res. Bull.* **2007**, *32*, 611–615. [[CrossRef](#)]
42. Fujita, T.; Konno, K.; Zhang, W.; Kumar, V.; Matsuura, M.; Inoue, A.; Sakurai, T.; Chen, M.W. Atomic-scale heterogeneity of a multicomponent bulk metallic glass with excellent glass forming ability. *Phys. Rev. Lett.* **2009**. [[CrossRef](#)] [[PubMed](#)]
43. Xi, X.K.; Li, L.L.; Zhang, B.; Wang, W.H.; Wu, Y. Correlation of atomic cluster symmetry and glass-forming ability of metallic glass. *Phys. Rev. Lett.* **2007**. [[CrossRef](#)] [[PubMed](#)]
44. Xi, X.K.; Sandor, M.T.; Liu, Y.H.; Wang, W.H.; Wu, Y. Structural changes induced by microalloying in Cu₄₆Zr_{47-x}Al₇Gd_x metallic glasses. *Scr. Mater.* **2009**, *61*, 967–969. [[CrossRef](#)]
45. Zhang, Y.; Chen, J.; Chen, G.L.; Liu, X.J. Glass formation mechanism of minor yttrium addition in CuZrAl alloys. *Appl. Phys. Lett.* **2006**. [[CrossRef](#)]

46. Saida, J.; Matsushita, M.; Inoue, A. Direct observation of icosahedral cluster in $Zr_{70}Pd_{30}$ binary glassy alloy. *Appl. Phys. Lett.* **2001**. [[CrossRef](#)]
47. Saksli, K.; Franz, H.; Jovari, P.; Klementiev, K.; Welter, E.; Ehnes, A.; Saida, J.; Inoue, A.; Jiang, J.Z. Evidence of icosahedral short-range order in $Zr_{70}Cu_{30}$ and $Zr_{70}Cu_{29}Pd_1$ metallic glasses. *Appl. Phys. Lett.* **2003**. [[CrossRef](#)]
48. Hentschel, H.G.E.; Moshe, M.; Procaccia, I.; Samwer, K.; Sharon, E. Microalloying and the mechanical properties of amorphous solids. 2015, arXiv:1510.03108.



© 2016 by the authors; licensee MDPI, Basel, Switzerland. This article is an open access article distributed under the terms and conditions of the Creative Commons by Attribution (CC-BY) license (<http://creativecommons.org/licenses/by/4.0/>).